A design methodology for quiet and long endurance MAV rotors

Ronan Serré, Hugo Fournier, Jean-Marc Moschetta

International Journal of Micro Air Vehicles

Article

A design methodology for quiet and long endurance MAV rotors

International Journal of Micro Air Vehicles
Volume 11: 1–14

DOI: 10.1177/1756829319845937
journals.sagepub.com/home/mav
SAGE

Ronan Serré, Hugo Fournier and Jean-Marc Moschetta

Abstract

Over the last 10 years, the use of micro air vehicles has rapidly covered a broad range of civilian and military applications. While most missions require optimizing the endurance, a growing number of applications also require acoustic covertness. For rotorcraft micro air vehicles, combining endurance and covertness heavily relies on the capability to design new propulsion systems. The present paper aims at describing a complete methodology for designing quiet and efficient micro air vehicle rotors, ranging from preliminary aerodynamic prediction to aeroacoustic optimization to experimental validation. The present approach is suitable for engineering purposes and can be applied to any multirotor micro air vehicle. A fast-response and reliable aerodynamic design method based on the blade-element momentum theory has been used and coupled with an extended acoustic model based on the Ffowcs Williams and Hawkings equation as well as analytical formulations for broadband noise. The aerodynamic and acoustic solvers have been coupled within an optimization tool. Key design parameters include the number of blades, twist and chord distribution along the blade, as well as the choice of an optimal airfoil. An experimental test bench suitable for non-anechoic environment has been developed in order to assess the benefit of the new rotor designs. Optimal rotors can maintain high aerodynamic efficiency and low acoustic signature with noise reductions in the order of 10 dB(A).

Keywords

Aeroacoustic, noise reduction, optimization, design

Received 12 December 2018; Revised received 13 March 2019; accepted 1 April 2019

Introduction

Designing a silent rotor goes through an aeroacoustic optimization, which implies understanding the aerodynamic phenomenon responsible for noise generation. Predicting the noise generated aerodynamically is relatively straightforward once detailed aerodynamic involved in the propulsion system is available through the use of direct noise computation or hybrid prediction. Aeroacoustic optimization in that framework is possible,[1,2] but demanding in terms of computational cost is not realistic in an industrial context. Lower fidelity, yet functional tools are then needed. Reduction in rotor noise has received important attention from the early ages of aeroacoustics.[3,4] It has yielded a lot of information and materials which allowed the development of low-fidelity models of sufficient accuracy. There are identical phenomena that occur in a helicopter rotor and an MAV rotor but the different noise sources do not contribute to the overall noise in the same amount. Detailed analysis of the aerodynamic characteristics has to be specifically dedicated to MAV rotors and low-fidelity models should be recalibrated or at least carefully selected. Aerodynamic and acoustic optimization of MAV rotors has been previously addressed for instance by Ormsbee and Woan[5] on a vortex line theory approach or by Gur and Rosen[6] but only tonal noise was considered. Noise reduction techniques were proposed, yielding promising conclusions, such as an unequal blade spacing to reduce tonal noise[7] or a boundary layer trip to remove the broadband noise.[8] This contribution presents a general methodology for reducing the noise

Institut Supérieur de l'Aéronautique et de l'Espace (ISAE-SUPAERO), Université de Toulouse, Toulouse, France

Corresponding author:
Ronan Serré, Institut Supérieur de l'Aéronautique et de l'Espace (ISAE-SUPAERO), Université de Toulouse, Toulouse Cedex 4 31055, France.
Email: ronan.serre@gmail.com

of MAV rotors while preserving or even increasing the endurance. A similar strategy has been followed by Wisniewski et al.[9] and Zawodny et al.[10] with models based on empirical data at relatively high Reynolds numbers and for symmetrical profile. The present study proposes a more general methodology and its originality lies in using low-fidelity albeit sufficiently accurate models of detailed acoustic spectrum applied with algorithms that modify the chord, the twist and the airfoil sections of MAV rotor blades. For the aerodynamic modeling, a widely spread low-fidelity model is used, based on the blade element and momentum theory (BEMT).[11] It is fast, reliable but yields a steady loading on the blades. Acoustics is intrinsically unsteady. Because of the relative motion between the spinning blades and a static observer, acoustic radiation can still be retrieved from a steady loading but it can only be tonal noise as a consequence of a periodic perturbation. As stated by Sinibaldi and Marino,[12] the acoustic spectrum radiated by rotors exhibits also a broadband part.[13,14] Low-fidelity broadband models are then needed in the optimization process to avoid designs where tonal noise is reduced and broadband noise then dominates. The acoustic modeling is realized in two steps: (i) an integral method based on the Ffowcs Williams and Hawkings (FWH) equation[15,16] gives the tonal noise radiated by the rotor from the steady loading yielded by the BEMT and (ii) analytical models based on the work of Roger and Moreau[17] estimate the broadband part of the acoustic spectrum. The optimization of the chord and the twist of the blades are yielded by a combination method, that is a systematic evaluation of the space of parameters. The optimization process is then to be seen as an analysis of all possible combinations rather than an actual optimization. Comparison with optimization algorithms will be addressed in a future work.

Aerodynamic modeling

Through a BEMT approach as described by Winarto,[11] local distributions of lift and drag and global thrust and torque are retrieved from local lift and drag coefficients of the blade element airfoil sections. As a result, knowledge of the aerodynamic polar of the considered airfoil section is essential to the process. Three strategies may be employed to this end: experimental,[18] numerical simulation[19] or numerical modeling (such as panel method in potential flow theory[20]). The last one is used in the present study for efficiency. Lift and drag coefficients and boundary layer data are extracted from Xfoil open-source software by Drela and Giles[20] and stored in the form of a database in a process independent of the optimization tool which only contains the BEMT for aerodynamic evaluation.

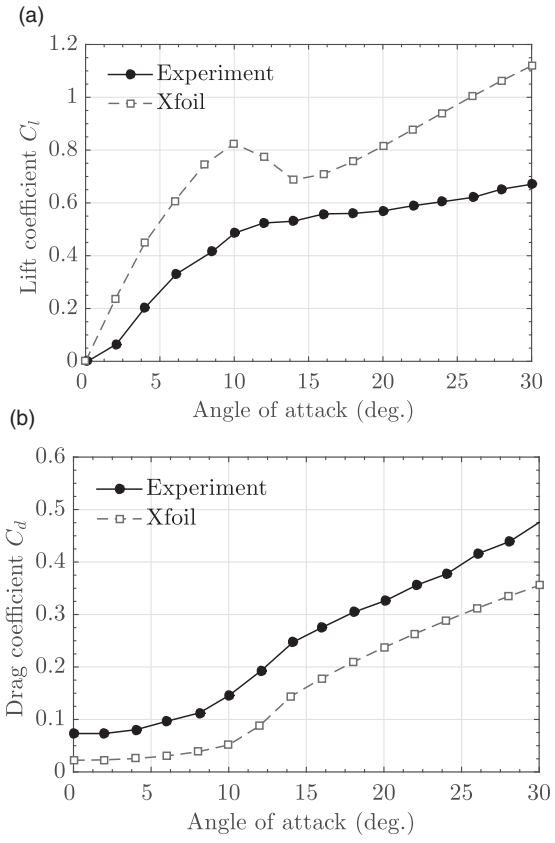

Figure 1. Aerodynamic coefficients between Xfoil prediction and experimental work by Martínez-Aranda et al.[18] for a NACA 0012 airfoil section at a Reynolds number $Re = 33{,}000$. (a) Lift coefficient. (b) Drag coefficient.

Figure 1(a) and (b) respectively show lift and drag coefficients predicted by Xfoil compared with experiment by Martínez-Aranda et al.[18] for a NACA 0012 airfoil section at a Reynolds number $Re = 33{,}000$. Xfoil prediction for the drag coefficient exhibits the same trend as the measurements although underestimated. The lift coefficient is clearly overestimated by Xfoil. Moreover, it exhibits a hump around a 10° angle of attack that is not found in the experimental work by Martínez-Aranda et al.[18] although it was also observed in the experimental work by Laitone.[21] Because the overestimation of the lift coefficient is higher than the underestimation of the drag coefficient, the optimization tool is expected to yield an overestimated thrust and a slightly underestimated torque in the investigated rotors. Figure 2 depicts boundary layer thickness δ on a NACA 0012 at Reynolds numbers $Re = 23{,}000$ and $Re = 48{,}000$ for a 6° angle of attack, compared with experiments by Kim et al.[22] The boundary layer behavior experimentally observed is dramatically ignored by Xfoil in the medium chord region which shows a monotonic trend. However, the values does

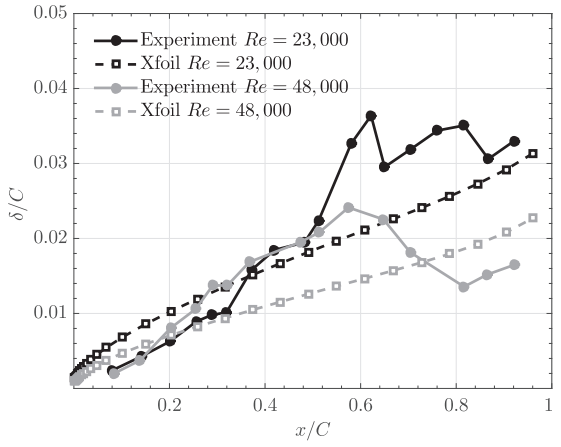

Figure 2. Boundary layer thickness on a NACA 0012 at Reynolds numbers $Re = 23{,}000$ and $Re = 48{,}000$ and a 6° angle of attack between Xfoil prediction and experiments by Kim et al.[22]

not exhibit too much discrepancy at the trailing-edge region where $x/C \sim 1$. Boundary layer data needed for the acoustic modeling are extracted from this region as will be seen in the next section. Xfoil prediction, with identified limitations, is considered satisfactory in this framework and is used to provide input data for the BEMT approach and broadband noise models. The validation of the BEMT tool has been addressed with high-fidelity numerical simulations and experiment.[23]

Acoustic modeling

The FWH equation is implemented in the time domain as expressed by Casalino[24] in the form known as Formulation 1A and applied on the blade surface.[25] Without any fluid volume inside the control surface, the quadrupole term representative of flow non-linearities is neglected but is believed to be of small contribution in this low-Reynolds, low-Mach number regime, typically encountered in MAV rotors.[12] The FWH equation then resumes to a surface integration eventually yielding the thickness and the loading noise. The main input parameters are the velocity of the blade element that influences the thickness noise and the force distributions that act on the loading noise. In addition, two sources of broadband noise are considered, based on Roger and Moreau:[17] the scattering of boundary layer waves by the trailing-edge and the ingestion of turbulence at the leading-edge. Roger and Moreau[17] mention a third source of broadband noise, that is the shedding of vortical eddies in the wake but this source is not yet considered. The main inputs for the trailing-edge noise model are a wall-pressure spectrum model as proposed by Kim and George[26] for instance and a spanwise correlation length as modeled by Corcos[27] tailored with a high-pass filter, in which the boundary layer data near the trailing-edge is necessary. This source of broadband noise is not expected to contribute significantly to the overall noise. However, its relevance is supported by the authors to prevent optimization cases where broadband noise overcomes the tonal noise, as was observed by Pagliaroli et al.,[28] especially if tonal noise is to be reduced. For the turbulence ingestion noise model, information on impinging turbulence is required. The driving parameters are the cross-correlated upwash velocity fluctuations spectrum that can be approximated with a von Kármán model[29] for instance, the mean intensity of the streamwise velocity fluctuations and the Taylor microscale as the turbulence length scale.[30] The latter is estimated by the optimization tool from the wake width created at the trailing-edge[31] that is believed to impinge the following blade's leading-edge following observation on LES-LBM simulation.[32] The broadband noise models estimate the noise in the form of a power spectral density, generated at the trailing-edge and leading-edge regions, from boundary layer data and turbulence statistics through a correlation function modified by a Doppler shift imposed by the relative motion between the source and the observer. For the optimization process, only one observer is considered, arbitrary located 45° above the plane of rotation, 1 m away from the center of rotation. Because the acoustic directivity yielded by the noise models exhibit a symmetrical behavior with respect to the plane of rotation, selecting an observer position 45° above or below that plane of rotation leads to the same conclusions, without representing the higher acoustic intensity that is radiated downward the plane of rotation in rotating machinery.[32] It is worth noting that formulation 1A of the FWH equation gives a singular value on the axis of rotation, while the trailing-edge noise model has its singularity on the plane of rotation. The singularity in the axis of rotation has also been reported by Lowson[33] and Mao et al.[34] Steady-loading noise (tonal noise) has zero efficiency on the rotation axis.

Optimization procedure

As stated in the introduction, relatively few optimization studies on low-Reynolds rotors have been published in spite of the general interest in MAVs and the recent observation that noise from MAVs is generally considered as annoying.[35] To demonstrate the feasibility of the optimization methodology and to identify the key parameters of the blade geometry allowing noise reduction, a step-by-step optimization of a two-bladed rotor is carried for increasingly complex blade geometries: (i) constant chord and constant twist with a NACA 0012 airfoil section; (ii) same constant chord and optimized twist with a NACA 0012 airfoil section;

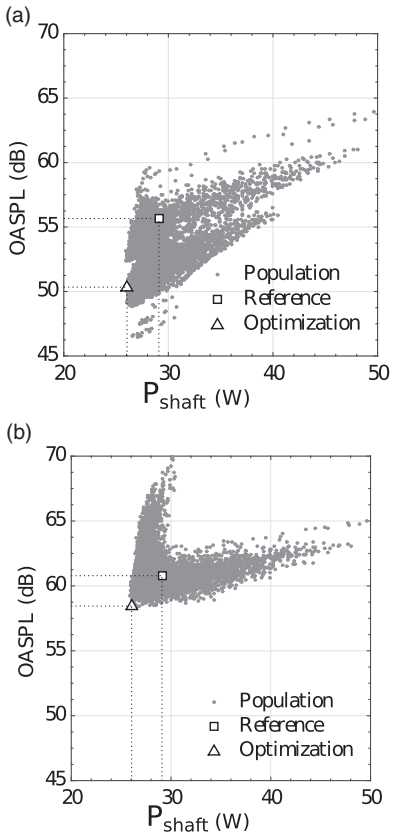

Figure 3. Representative optimization process through combination method. Population, reference blade and best optimized individual. (a) With tonal noise. (b) With broadband noise.

(iii) optimized chord and twist with a NACA 0012 airfoil section and (iv) previous blade geometry with optimized airfoil sections at three radial positions based on local Reynolds number and angle of attack. The successive optimizations occur at iso-thrust, that is to say, the rotational speed is adapted so that the optimized rotors deliver the same thrust, set at 2 N, to represent MAVs in hover. For each case, the optimized geometry is selected on the Pareto front given by the optimization tool to minimize both the aerodynamic power P_{shaft} and the OASPL at one specific observer position. Figure 3 illustrates the result of a representative optimization process. The total population is depicted and the initial geometry (reference blade) and the best optimized one are highlighted. That best optimized geometry has been selected to minimize the aerodynamic power Ap and the broadband OASPL. Figure 3(a) plots the individuals evaluated with the sole tonal noise, while Figure 3(b) plots the same individuals but evaluated with the broadband noise models. The best optimized geometry that is highlighted on both Figure 3(a) and (b) has the lowest P_{shaft} and the lowest broadband OASPL. However, that selected geometry does not have the lower tonal OASPL, emphasizing the necessity to take into account the sources of broadband noise in the acoustic modeling for optimization purposes. In figure 3(b), it is worth noting that the whole population is directed towards both a lower P_{shaft} and a lower OASPL, like a swarm. Figure 3 illustrates the possibility to enhance both aerodynamic and acoustic characteristics of MAV rotors. The blade chord and twist laws are parameterized by Bézier curves considering control points in four sections along the blade span giving eight variables. However, to ensure lift at blade tip reaches zero to yield a minimum induced velocity, the twist at the fourth control point is imposed at zero eventually giving seven variables. Each variable may take five values giving five[7] individual evaluations. Note that the twist angle β is defined with respect to the plane of rotation. A multi-objective selection is applied to express the Pareto front according to the lower aerodynamic power P_{shaft} and lower overall sound pressure level (OASPL). The optimization of the airfoil sections is carried out in a second step through another process, here with actual use of optimization algorithm, for it is applied once local distribution of Reynolds numbers and angle of attacks are known on a rotor with optimized chord and twist distribution laws. Airfoil shapes are determined using CST parametrization[36] with 12 coefficients. The objective is to maximize the lift-to-drag ratio through NSGA-II evolutionary algorithm[37] with a population of about 100 individuals. The final evaluation is achieved after 55 generations. Three positions along the span were selected for the aerofoil optimization and the aerofoil sections in-between, in the spanwise direction were built from spline interpolation. A schematic view of the organization of the optimization tool is provided in Figure 4. The blade geometries are then built using SLA technology on a FormLabs 3D-printer with a 50 μm vertical resolution for experimental purposes. Figure 5 depicts a typical printed rotor. The printed rotors are manually grinded to remove the supports from the printer and are balanced on a static equilibrium axis. The tip radius is the same for all the rotors and is set at $R = 0.0875$ m, imposed by the printing volume allowed by the 3D-printer and selected as a representative tip radius found in 7 inches commercial rotors for MAVs. At the time the optimizations were carried out, only the trailing-edge noise model was active. The turbulence interaction noise model was under investigation as it needed calibration.[32]

Numerical results

The successive configurations show an increased twist, along with an increase of the chord for the third

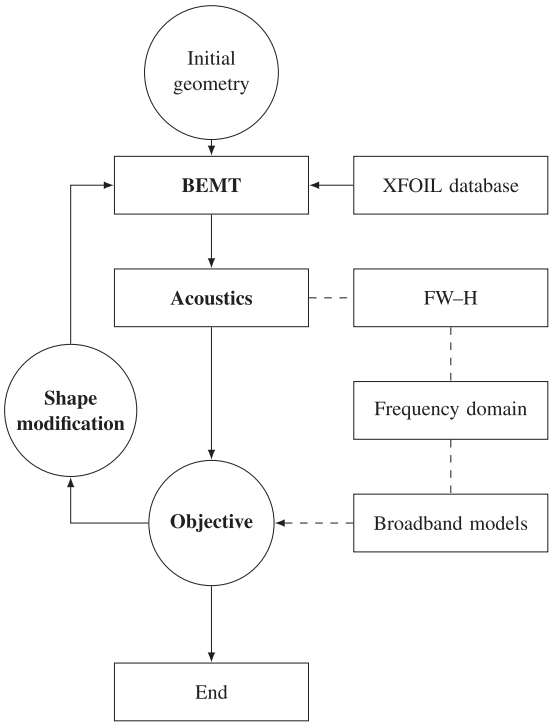

Figure 4. Diagram of operations of the numerical optimization tool.

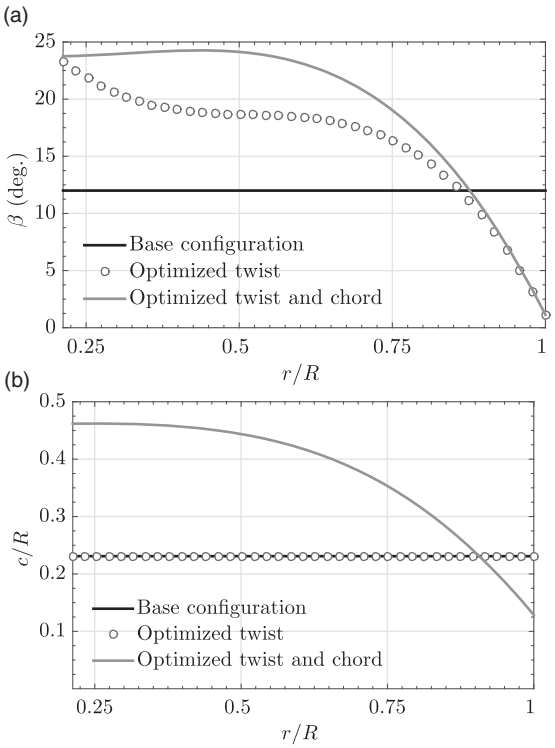

Figure 6. Twist and chord distribution laws of the successive rotors. (a) Twist. (b) Chord.

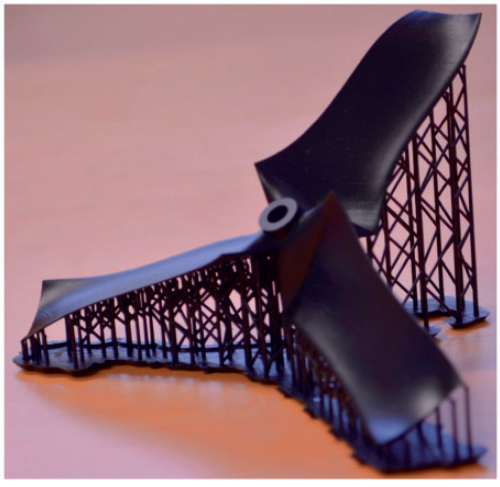

Figure 5. A representative, 3D-printed rotor.

optimization. For that optimized rotor, the chord monotonically decreases with the span (Figure 6(a)), while the twist is high at the hub, slightly increases at mid-span before reaching a minimal value at the tip (Figure 6(b)). The span direction and the chord are normalized by the tip radius R. The optimized airfoil sections at three radial positions are depicted in Figure 7. They were obtained by an optimization process as previously described to maximize the

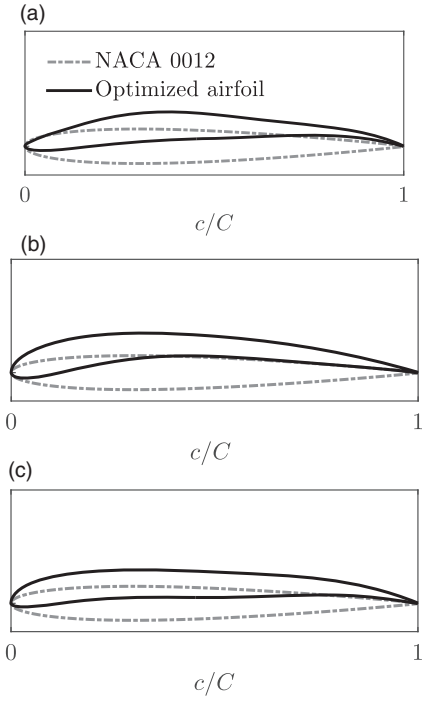

Figure 7. Optimized airfoil sections for the fourth rotor compared with the base configuration (NACA 0012). (a) $r/R = 1.0$ ($Re = 42{,}000$). (b) $r/R = 0.5$ ($Re = 82{,}000$). (c) $r/R = 0.1$ ($Re = 32{,}000$).

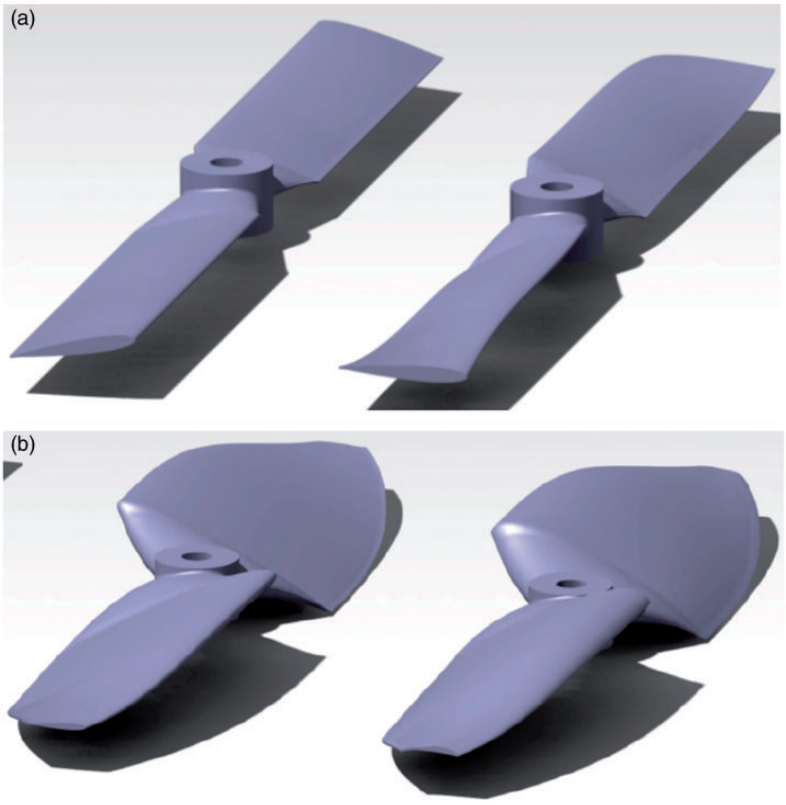

Figure 8. CAD representation of the four rotors considered in the present study. (a) Initial rotor (base configuration, left) and optimized twist (right). (b) optimized twist and chord (left) and additional optimized airfoil sections (right).

lift-to-drag ratio at the local Reynolds number and for an average of three angles of attack around the values at the specified radial positions. They are all thinner than the reference one and cambered as can be expected for low-Reynolds number aerodynamics. The airfoil section near the tip region ($r/R = 1$) exhibits a bump on the suction side, that might indicate an adaptation to separation phenomenon for a very specific local Reynolds number. It might be avoided if the airfoil optimization is made by taking the average result over different Reynolds numbers along with the average in the angles of attack. A CAD representation of the four rotors is depicted in Figure 8. Figure 9(a) and (b) shows lift and drag coefficients, respectively, distributed along the span for the successive blades. The lift coefficient is successively increased with a maximum localized around 75% of the blade radius. The drag coefficient is also increased although less intensively with a maximum value localized around 65% of the blade radius. The lift coefficient is seen to have been multiplied by three, while the drag coefficient has been multiplied by two. The gain in aerodynamic efficiency for the successive optimizations yields a diminution of the rotational speed required to deliver the thrust objective set at 2 N, as will be presented in Table 1 and discussed in the next section, resulting in a diminution of the blade passing frequency (BPF). The tendency of the optimizations to move the BPF towards low frequencies has an effect on the noise reduction because low frequencies are less perceived by the human ear. As the optimizations were carried with the sole trailing-edge noise model active, Figure 10 is presented to assess the ability of the optimization tool to reduce the overall noise nevertheless, even with this sole source of broadband noise. In Figure 10, the blade element contribution to overall noise is shown for the four configurations from the trailing-edge noise model (Figure 10(a)) and the turbulence ingestion noise model (Figure 10(b)). For the base configuration, the blade element contribution increases almost linearly towards the tip region according to a Reynolds number effect. The three successive optimizations have a zero twist angle at the tip and it results in a drastically reduced radiated noise from the trailing-edge near the tip region. The third and fourth optimization cases express a lower radiated noise for each blade element although its chord and twist distribution laws are higher than the second optimization case. The airfoil section optimization increases that tendency. To investigate the noise reduction yielded by the optimization tool

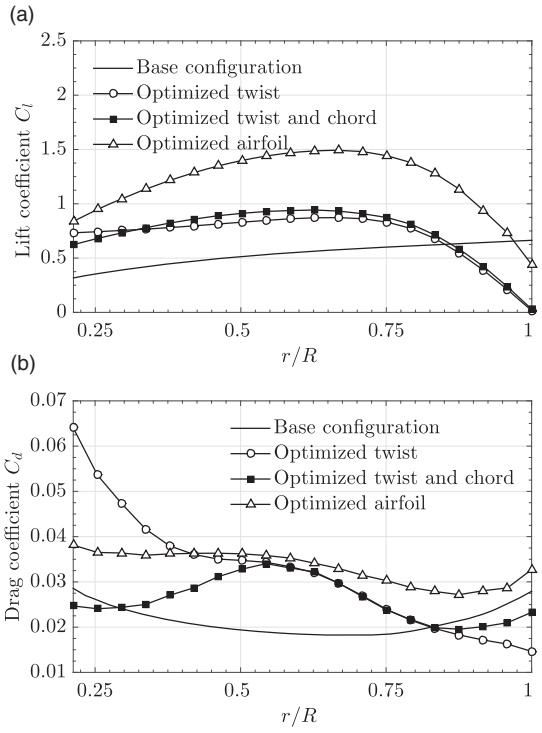

Figure 9. Spanwise aerodynamic coefficient distributions of the successive rotors for a 2 N thrust. Numerical prediction. (a) Lift coefficient. (b) Drag coefficient.

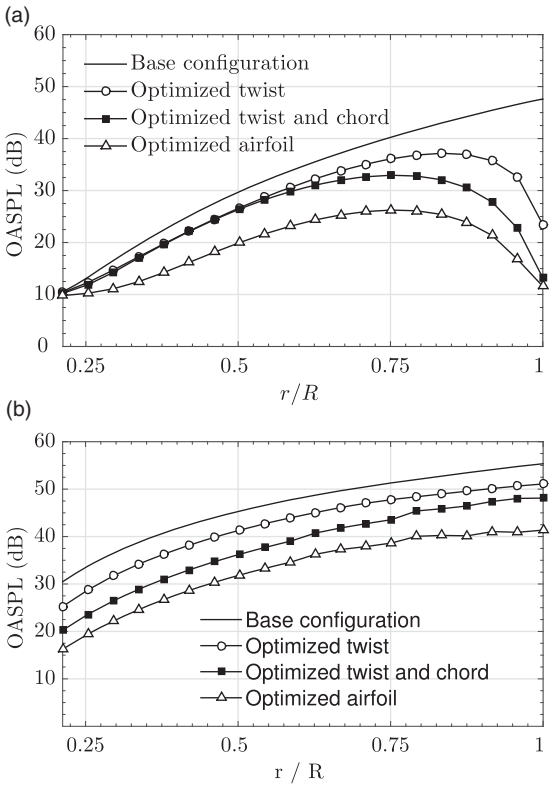

Figure 10. Spanwise blade element contribution to the overall sound pressure level (OASPL) for a 2 N thrust for the successive rotors. Numerical prediction. (a) Trailing-edge noise. (b) Turbulence ingestion noise.

Table 1. Rotational speeds and corresponding blade passing frequency for a 2 N thrust between numerical prediction and experiment for the four successive rotors.

	Numerical	Experimental
Baseline	9310 r/min (310 Hz)	9800 r/min (325 Hz)
Twist	7630 r/min (255 Hz)	8400 r/min (280 Hz)
Chord and twist	6010 r/min (200 Hz)	6650 r/min (220 Hz)
Airfoil	4880 r/min (165 Hz)	5450 r/min (180 Hz)

for the successive rotors, Figure 11(a) and (b) shows the A-weighted sound power level predicted by the trailing-edge and the turbulence ingestion noise models, respectively. The A-weighted sound power level is computed following the guideline set by the ISO 3746 : 1995 standard in third octave bands for the successive rotors at a 2 N thrust. The important difference in magnitude between the two numerical models is noteworthy. The optimization tool suggests that turbulence ingestion is a more intense source of noise than trailing-edge noise and can overcome the main tonal component at the first BPF. From the two noise models, noise reduction is observed for the successive optimizations. The main tonal noise component that occurs at the first BPF is reduced for each optimization case, up to 25 dB(A) with the fourth rotor as observed in both Figure 11(a) and (b). From the second optimization, the trailing-edge noise is dramatically reduced and the following optimizations increase that tendency (Figure 11(a)). The turbulence ingestion noise is also systematically reduced (Figure 11(b)).

Experiment

The experiment took place in a rectangular room, not acoustically treated, of dimensions $(l_1 \times l_2 \times l_3) = (14.9 \times 4.5 \times 1.8)$ m^3. The aerodynamic forces are retrieved from a five components balance. The aerodynamic measurements are validated against the UIUC online database on a commercial Graupner SlimProp 9x6 propeller published in Brandt and Selig.[38] The thrust and the torque coefficients are shown in Figure 12 for several rotational speeds, according to definitions from Leishman[39] as

$$C_t = \frac{T}{\frac{1}{2}\rho(\omega R)^2 \pi R^2} \;\; ; \;\; C_q = \frac{Q}{\frac{1}{2}\rho(\omega R)^2 \pi R^3}$$

where T is the thrust, Q is the torque, ρ is the ambient density, ω is the rotational frequency and R is the rotor

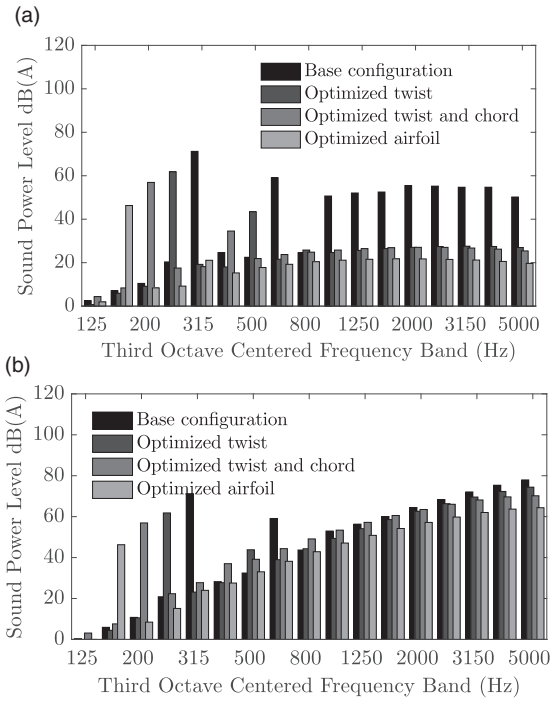

Figure 11. Sound power level of the acoustic spectrum of the successive rotors for a 2 N thrust. Numerical prediction from broadband noise models. (a) Trailing-edge noise. (b) Turbulence ingestion noise.

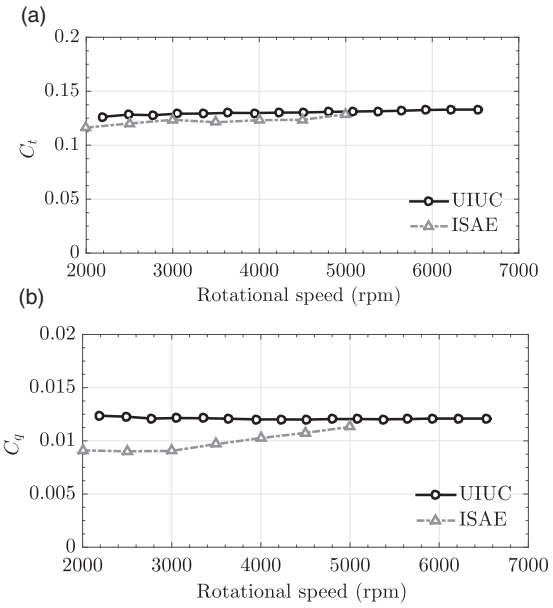

Figure 12. Aerodynamic coefficients of a commercial Graupner SlimProp 9x6 propeller. Measurements from ISAE-SUPAERO and UIUC.[38] (a) Thrust coefficient. (b) Torque coefficient.

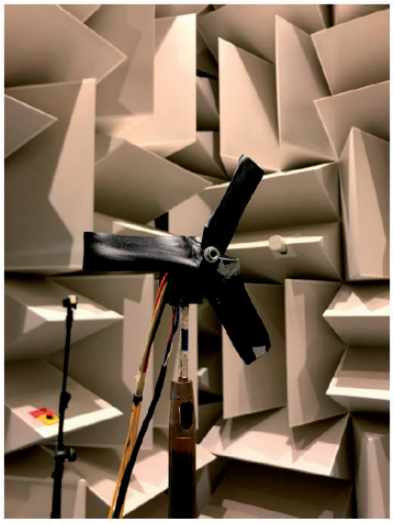

Figure 13. Experimental set-up in the anechoic chamber used to validate the ISO standard. The five components aerodynamic balance is below the motor driving the rotor.

tip radius. The thrust coefficient is coherent with the measurements from UIUC but the torque is underestimated with respect to experiments by Brandt and Selig[38] for the lowest rotational speeds, eventually leading to a possible overestimation of the figure of merit. The measurements at ISAE-SUPAERO were not carried beyond 5000 r/min for it exceeded the balance capacity with forces beyond 3 N. The A-weighted sound power levels and the total A-weighted acoustic power are computed according to ISO 3746 : 1995 standard with five measurement points approximately 1 m around the rotor on Brüel & Kjær $1/2''$ free-field microphones and a Nexus frequency analyzer with a frequency resolution of 3.125 Hz. The distance between the source and the microphones approximately represents five rotor diameters. Four of the microphones are positioned in the form of a circle parallel to the ground whose center is aligned with the rotor center of rotation. The fifth microphone is located in the plane of rotation. The rotor has an horizontal axis of rotation. The validity of the ISO standard is assessed with sound measurements in an anechoic environment, only recently available at ISAE-SUPAERO. This new facility is a cube of 9 m wide with 1, 20 m long wedges on the walls. The lower cut-off frequency is 90 Hz, while the upper one is 16,000 Hz. Figure 13 illustrates the experimental set-up in the anechoic chamber. Comparisons are plotted between measurements carried in the standard room and measurements carried in the anechoic chamber on the total A-weighted acoustic power (Figure 14) for a representative MAV rotor. The validity of the ISO 3746 : 1995 standard to account for non-anechoic environment is satisfying. In spite of a 10 dB gap observed between the OASPLs of the two measurements on narrow band power spectral

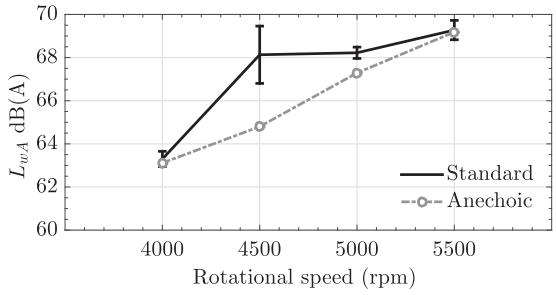

Figure 14. Acoustic power according to ISO 3746 : 1995 standard of a representative MAV rotor. Comparison between measurements in the standard room and in the anechoic chamber.

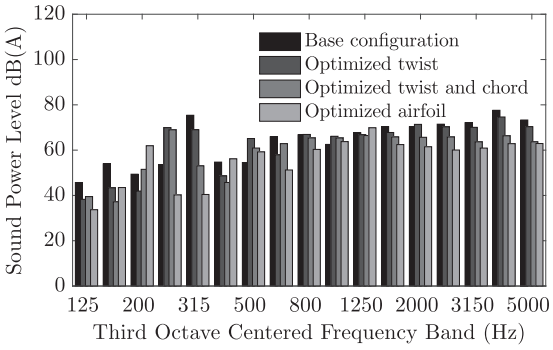

Figure 16. Sound power level of the acoustic spectrum of the successive rotors for a 2 N thrust. Experiment.

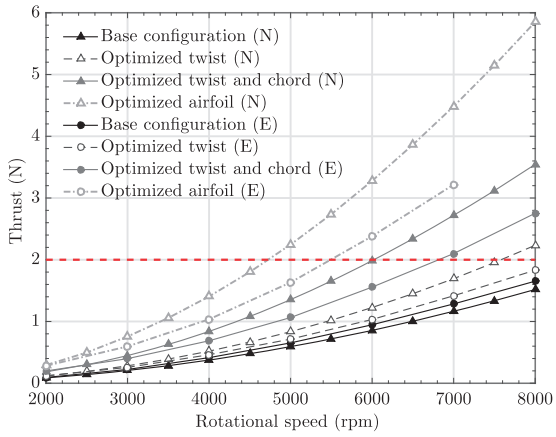

Figure 15. Thrust evolution with rotational speed of the successive rotors from numerical prediction and experiment. The horizontal dash line (red) indicates thrust objective at 2 N. N: numerical predictions. E: experiment.

densities, the total acoustic powers are consistent. The severe discrepancy between the two acoustic powers at 4500 r/min, at the very same moment where the standard deviation is the highest, is believed to be a consequence of installation effects. In the standard room, the rotor is close to the ground. Ingestion of vorticity filaments by the rotor causing distortion effects is expected. Figure 15 exhibits thrust measurements and numerical predictions for the four successive configurations and several rotational speeds. The thrust is generally estimated by the optimization tool as was expected from the discussion proposed in the aerodynamic modeling section because of the overestimation of the lift coefficient in Xfoil software. Measurements and numerical predictions express the same trend, a higher discrepancy observed for the third and fourth optimizations notwithstanding. Such discrepancy might be attributed to Xfoil inability to accurately predict the aerodynamic loads on exotic aerofoil shapes such as the optimized aerofoil sections. Wind tunnel experiments should be carried on the optimized aerofoil and compared with Xfoil computations to further document that point. The rotational speeds to reach the thrust objective of 2 N and the corresponding blade passing frequencies are presented in Table 1 for the numerical prediction and the experiment. Table 1 clearly shows that the main effect of the successive optimizations is to reduce the rotational speed needed to reach the thrust objective and lower the BPF. Figure 16 shows the sound power level computed according to ISO 3746 : 1995 standard in the third octave bands for the successive rotors at a 2 N thrust from the experiment. It can be directly compared with Figure 11(a) and (b). Noise reduction is effectively observed, although less than the noise reduction observed from numerical predictions (Figure 11(a) and (b)). In the experiment, the main tonal component at the first BPF is reduced by a maximum of 15 dB(A) between the base configuration and the fourth rotor, where the optimization tool predicted a noise reduction by 25 dB(A). Noise reduction occurs in every frequency band. Comparing Figure 16 with Figure 11(a) and (b) suggests evidences that turbulence ingestion noise might be the dominant source of broadband noise. A slight overestimation by the optimization tool at high frequencies is, however, to be expected.[32]

Results and discussion

Figure 17 shows the sound power level computed according to ISO 3746 : 1995 standard in third octave bands for the final optimized rotor at a 2 N thrust from measurements and numerical predictions (trailing-edge and turbulence ingestion noise models). Although it is not possible to distinguish the broadband component from the tonal component on a third octave spectrum, it is clear that the low frequencies do not contribute to the OASPL. The high frequency content from the

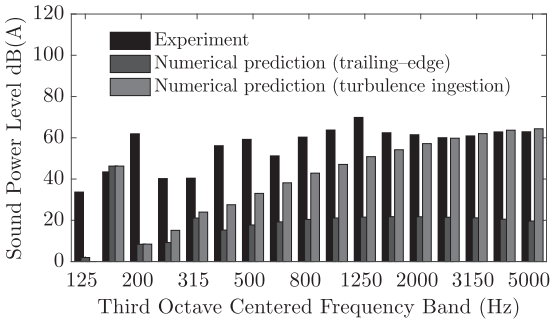

Figure 17. Sound power level of the acoustic spectrum of the final optimized rotor for a 2 N thrust.

numerical prediction reaches the level of the OASPL then supporting the idea that broadband noise prediction is relevant to the design of MAV rotors. The trailing-edge noise model predicts sound power levels that do not reach the sound power levels observed in the experiment. On the contrary, the turbulence ingestion noise model seems able to predict accurately the broadband components of the sound power spectrum. The exceeding sound power levels seen from the experiments are tonal noise at the BPF and its harmonics. It is believed to be a consequence of unsteady loading. As a result, it is not retrieved by the optimization tool as a consequence of the steady aerodynamic input data. Unsteady loading increases the strength of the first BPF, induces sub-harmonic peaks and high frequency broadband content. Such high-frequency broadband content is a consequence of the typical small wavelength of turbulence found in this configuration[32] that impinges the leading edge and induces force fluctuations on the blade. Hence, it is observed that unsteady loading is the responsible mechanism for most of the noise produced in this configuration and leads the turbulence ingestion noise to be the dominant source of broadband noise. This is consistent with the work of George and Chou.[40] Additional analysis on broadband and tonal components is needed and will be addressed in a future work from measurements in anechoic environment. In the context of a steady loading framework, turbulence ingestion noise model such as the model proposed by Roger and Moreau[17] is then essential to estimate most of the acoustic energy radiated by MAV rotors in hover. In Figure 17, the first BPF is particularly higher in the experiments. In addition to unsteady loading, it may more specifically be a consequence of installation effects. The experimental test bench holds the rotor in such a way that its axis of rotation is parallel to the ground. As a consequence, a stand that includes the aerodynamic balance is mounted vertically, behind the rotor and it might yield additional noise radiation at the BPF and its harmonics. Moreover, the

Table 2. Aerodynamic power P_{shaft} in Watts and total acoustic power L_{wA} in dB(A) for the four successive rotors for a 2 N thrust.

Units: Watts (W)	N: P_{shaft}	E: P_{shaft}	
Baseline	19.6	**25.2**	
Twist	17.2	22.1	
Chord and twist	17.9	23.1	
Airfoil	16.9	**21.3**	
Units: dB(A)	NTE: L_{wA}	NTI: L_{wA}	E: L_{wA}
Baseline	72.0	85.0	**83.3**
Twist	61.9	81.2	81.3
Chord and twist	57.0	77.1	76.6
Airfoil	46.6	71.1	**74.5**

N: numerical prediction; E: experiment; TE: trailing-edge noise model; TI: turbulence ingestion noise model.

Note: The boldface values (Pshaft and LwA of both the baseline and the airfoil optimization) highlight the improvement yielded by the optimization. We chose to put in bold the baseline and the final optimization to emphasize the noise reduction and the power.

motor radiates its own noise. A sharp tonal peak can be identified on narrow band measurements at a passing frequency based on the number of magnetic poles in the motor but broadband noise possibly yielded by the motor cannot be identified so far. Additional noise may also be provided by the fact that the motor rotational speed is actually fluctuating but standard deviation is found to be approximately 2% around the aimed rotational speed. As long as these additional sources of noise are not isolated, a straightforward identification of the sources of noise in the rotor cannot be carried out from a typical narrow-band frequency spectrum. This is left for future work. Eventually, the following tables exhibit comparison between numerical predictions and experiment on the aerodynamic power and on the total acoustic power (Table 2). The aerodynamic power, defined as $A_p = \omega Q$ where Q is the torque and ω is the rotational frequency, is underestimated by the optimization tool by almost 6 W but the power reduction is higher in the experiment (Table 2). That underestimation was expected from the underestimation of the drag coefficient by Xfoil software as discussed in the aerodynamic modeling section on page §. The total acoustic power is underestimated by the optimization tool with the trailing-edge noise model but is efficiently predicted by the optimization tool with the turbulence ingestion noise model, a slight underestimation for the final configuration notwithstanding. As a result, the reduction of the total acoustic power is amplified by the numerical method (Table 2). The general trend of the optimization process as shown in Table 2 is promising: a reduction by 9 dB(A) in the total acoustic power reduction is experimentally observed together

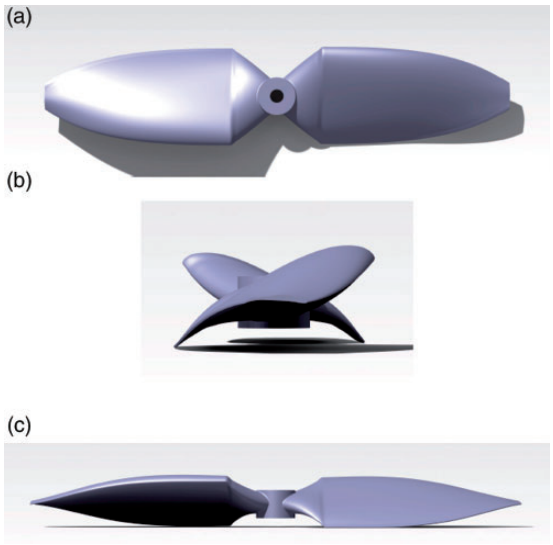

Figure 18. CAD representation of the optimized rotor. It radiates 10 dB(A) less and consumes 4 W less for the same thrust production. (a) Top view. (b) Side view. (c) Front view.

with a reduction by 4 W in the aerodynamic power and that is achieved at a minimum cost thank to the optimization tool. Closer views of the most efficient rotor of the successive configurations are shown in Figure 18.

Designing quiet and long endurance MAVs

From materials exposed in this contribution, general recommendations can be expressed for the design of quiet and efficient MAV rotors. This contribution aimed at highlighting the effects of twist, chord and airfoil section on noise and aerodynamic power. Other parameters that contribute to reduce the noise in MAVs and that have not been addressed in this contribution are for instance the tip radius and the number of blades. Both parameters would allow to increase the aerodynamic efficiency and lower the rotational speed. However, there is always a limit. Beyond the limit in the tip radius, the Mach number will increase which in turn will increase the radiated acoustic power. Loss in acoustic compactness should also be avoided for it will increase the strength of the sources of noise, although MAV should not be concerned: the rotational speed is generally about 5000 r/min, inducing fundamental frequency around 300 Hz and yielding a dominant wavelength of about 1 m. Beyond the limit in the blade number, blade-to-blade interactions and high intensity wake will start to occur eventually increasing the turbulence ingestion noise and as a consequence, the radiated acoustic power. In addition, an odd number of blades is perceived as less annoying as mentioned in a recent study on psychoacoustics.[35] Three-bladed rotors

Figure 19. Indoor flying platform at ISAE-SUPAERO and flight test of MAV with optimized rotor.

are generally considered as a good candidate. Destructive interference between the blades is not believed by the authors to be possible at least in a steady loading framework: each blade will act in the same way but with a time delay of $2\pi/B\omega$, where B is the blade number and ω is the rotational frequency. Destructive interference will occur if and only if this time delay equals half of the main acoustic wave period. However, this practically never holds: $2\pi/B\omega \neq 1/2B\omega$, except for high blade numbers B or high rotational frequencies ω. As an additional parameter for the design of quiet and efficient MAV rotors, a specific leading-edge design[41,42] might help reach higher levels of noise reduction because turbulence ingestion noise is believed to be the dominant source of broadband noise in MAV rotors and is generated in the vicinity of the leading-edge. In addition, the motor selection should be a part of these design recommendations. Brushless motors that are currently used for MAV propulsion have a mechanical efficiency that evolves with the rotational speed as stated by Bronz.[43] Once the optimum rotor geometry has been selected, the motor can be selected to provide the highest mechanical efficiency for the specific optimum rotational speed imposed by the rotor. The general guidelines for quiet and long endurance MAVs are now proposed as follows: (i) consider three-bladed rotors with the highest tip radius; (ii) optimize the chord and the twist distribution laws combined to minimize the OASPL and the aerodynamic power for a thrust objective; (iii) optimize the airfoil sections to maximize the lift-to-drag ratio for a given Reynolds number and angle of attack; (iv) modulate the chord distribution law with a *sine* function described in terms of wavelength and amplitude and (v) eventually select the most appropriate motor from the operating conditions of the now optimized rotor. These recommendations have been brought to a flight test in ISAE-Supaero which demonstrated the possibility to effectively reduce noise (Figure 19). A first flight test was carried with a commercially available rotor, the

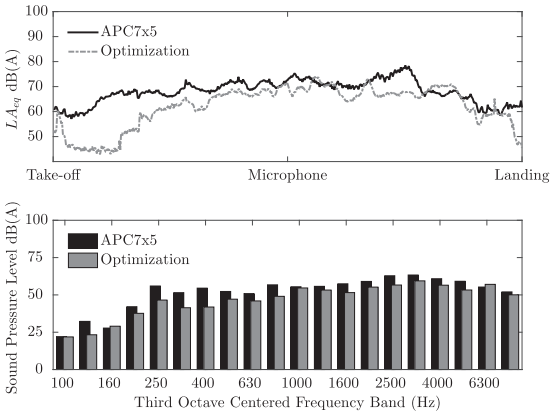

Figure 20. Noise measurements during the flight test. **Top:** equivalent sound pressure level in the time domain with reference to the flight path. **Bottom:** averaged sound pressure level in third-octave bands.

APC7x5 and a second one with the optimized rotor. The reader is referred to Serré et al.[32] for the characteristics of both the reference and the optimized rotors. In the flight test depicted in Figure 19, the MAV was programmed to follow a simple path: take-off to reach 2 m high, fly steady on a straight line, stop and land. A sound level meter was localized in the middle of that path at the same height, following a fly-by approach. The measurements from the sound level meter are shown in Figure 20 for the equivalent sound pressure level in the time domain (LA_{eq}) and the sound pressure level in the third-octave bands. Figure 20 suggests that noise reduction is effective and occurs in every situation along the flight path and in every frequency band.

Conclusion

This contribution has presented an innovative blade design methodology to reduce the noise and increase the endurance of MAVs in hover with fabrication method and experimental validation in non-anechoic environment. Acoustic models for tonal and broadband noise are implemented in a general low-cost numerical tool with satisfying accuracy. The methodology is mainly based on low-order computational tools and applied for successive modifications of the chord and twist radial distribution laws and airfoil sections to identify the best individuals. The successive optimizations presented in this study showed that adapting only the twist increases the lift but increases the drag coefficient more severely, while adapting both chord and twist significantly decreases the drag without affecting the lift. Adapting the airfoil sections gives an important additional increase of lift without significant drag increase. On the acoustic reduction, the main effect of the optimizations is seen to provide higher aerodynamic efficiency allowing reduction of the rotational speed, which has three effects: (i) lower the tip Mach number driving the intensity of the radiated acoustic energy, (ii) lower the main frequency of the tonal noise and (iii) weaken the intensity of the small turbulent eddies that create turbulence ingestion noise at high frequencies. The consequence is a direct reduction in the radiated acoustic energy. This study suggests that unsteady loading is responsible for most of the noise produced by MAV rotors in hover. It strengthens the first BPF, induces subharmonic peaks and high frequency broadband content that is turbulence ingestion noise, considered as the dominant source of broadband noise in such configurations. The model for this source of noise discussed in this study is a good candidate for relatively accurate prediction of the total acoustic power radiated by MAV rotors in hover and should be seriously considered for aeroacoustic optimization purposes. Further investigations on other sources of broadband noise are left for future work. The acoustic estimation from unsteady aerodynamic input data should be thoroughly investigated to gain new insight in aeroacoustic prediction and optimization. An accurate modeling of unsteadiness could alleviate the problem of broadband noise prediction at high frequencies but the resultant increase of computational cost might possibly be prohibitive for an optimization process. Key parameters driving the acoustic power radiated from MAV rotors have been highlighted and general recommendations have been suggested, including blade number, rotor tip radius, chord and twist distribution laws, airfoil sections and alternative designs. This study has contributed to the validation and the demonstration of an efficient blade design methodology for reducing rotor noise and increasing endurance of MAVs. The noise from a representative MAV rotor has been reduced by 10 dB(A). The optimization tool and the experimental protocol described in the present paper are suitable for engineering purposes. Reducing the noise from MAVs in hover can be achieved without expensive means. High-order computational tools could then be saved for further reduction of noise levels.

Acknowledgements

The authors thank Rémy Chanton for the set-up of the aerodynamic balance and Sylvain Belliot for the rapid prototyping and are grateful to Marc C. Jacob, Vincent Chapin and Sébastien Prothin for helpful discussions.

Declaration of conflicting interests

The author(s) declared no potential conflicts of interest with respect to the research, authorship, and/or publication of this article.

Funding

The author(s) disclosed receipt of the following financial support for the research, authorship and/or publication of this article: This work has been partly supported by the French Procurement Armement agency under grant DGA/MRIS n° 2012.60.0012.

ORCID iD

Ronan Serré https://orcid.org/0000-0003-4970-0780

References

1. Pagano A, Barbarino M, Casalino D, et al. Tonal and broadband noise calculations for aeroacoustic optimization of propeller blades in a pusher configuration. In: *15th AIAA/CEAS aeroacoustics conference*, Miami, Florida, May 2009.
2. Pednekar S, Ramaswamy D and Mohan R. Helicopter rotor noise optimization. In: *5th Asian-Australian rotorcraft forum*, Singapore, November, 2016.
3. Farassat F. *Theory of noise generation from moving bodies with an application to helicopter rotors*. NASA, Technical Report R-451, 1975.
4. Succi GP. Design of quiet efficient propellers. *SAE Transc* 1979; 881: 2039–2052.
5. Ormsbee AI and Woan CJ. Optimum acoustic design of free running low speed propellers. In: *Aircraft systems and technology meeting*, Seattle, WA, 22–24 August 1977. [AIAA Paper].
6. Gur O and Rosen A. Optimization of propeller based propulsion system. J Aircraft 2009; 46: 95–106.
7. Cattanei A, Ghio R and Bongiovì A. Reduction of the tonal noise annoyance of axial flow fans by means of optimal blade spacing. Appl Acoust 2007; 68: 1323–1345.
8. Leslie A, Wong KC and Auld D. Broadband noise reduction on a mini-UAV propeller. In *14th AIAA/CEAS aeroacoustics conference*.
9. Wisniewski CF, Byerley AR, Heiser WH et al. Designing small propellers for optimum efficiency and low noise footprint. In: *33rd AIAA applied aerodynamics conference*, Dallas, Texas, June 2015 [AIAA-2015-2267].
10. Zawodny NS, Douglas Boyd Jr D and Burley CL. Acoustic characterization and prediction of representative, small-scale rotary-wing unmanned aircraft system components. In: *72nd AHS annual forum*, West Palm Beach, Florida, May 2016.
11. Winarto H. BEMT algorithm for the prediction of the performance of arbitrary propellers. Melbourne: The Sir Lawrence Wackett Centre for Aerospace Design Technology, Royal Melbourne Institute of Technology, 2004.
12. Sinibaldi G and Marino L. Experimental analysis on the noise of propellers for small UAV. Appl Acoust 2013; 74: 79–88.
13. Goldstein ME. Aeroacoustics. USA: McGraw-Hill Book Co., 1976.
14. Blake WK. Mechanics of flow-induced sound and vibration. USA: Academic Press, Inc., 1986.
15. Ffowcs Williams JE and Hawkings DL. Sound generation by turbulence and surfaces in arbitrary motion. Philos Transac R Soc Lond 1969; 264: 321–342.
16. Farassat F and Succi GP. A review of propeller discrete frequency noise prediction technology with emphasis on two current methods for time domain calculations. J Sound Vibration 1980; 71: 399–419.
17. Roger M and Moreau S. Extensions and limitations of analytical airfoil broadband noise models. Int J Aeroacoust 2010; 9: 273–305.
18. Martínez-Aranda S, García-González AL, Parras L et al. Comparison of the aerodynamic characteristics of the NACA0012 airfoil at low-to-moderate Reynolds numbers for any aspect ratio. Int J Aerosp Sci 2016; 4: 1–8.
19. Morgado J, Vizinho R, Silvestre MAR et al. XFOIL vs. CFD performance predictions for high light low Reynolds number airfoils. Aerosp Sci Technol 2016; 52: 207–214.
20. Drela M and Giles MB. Viscous-inviscid analysis of transonic and low Reynolds number airfoils. AIAA J 1987; 25: 1347–1355.
21. Laitone EV. Wind tunnel tests of wings at Reynolds numbers below 70 000. Exp Fluids 1997; 23: 405–409.
22. Kim DH, Yang JH, Chang JW, et al. Boundary layer and near-wake measurements of NACA 0012 airfoil at low Reynolds numbers. In: *47th AIAA aerospace sciences meeting*, Orlando, Florida, January 2009. [AIAA-2009-1472]
23. Gourdain N, Serré R, Jardin T, et al. Analysis of the flow produced by a low-Reynolds rotor optimized for low noise applications. part I: aerodynamics. In: *43rd European rotorcraft forum*, Milan, Italy, September 2017.
24. Casalino D. An advanced time approach for acoustic analogy predictions. J Sound Vib 2003; 261: 583–612.
25. Nana C, Moschetta JM, Bénard E, et al. Experimental and numerical analysis of quiet MAV rotors. In: *50th 3AF international conference on applied aerodynamics*, Toulouse, France, April 2015.
26. Kim YN and George AR. Trailing-edge noise from hovering rotors. AIAA J 1982; 20: 1167–1174.
27. Rozenberg Y, Roger M and Moreau S. Rotating blade trailing-edge noise: experimental validation of analytical model. AIAA J 2010; 48: 951–962.
28. Pagliaroli T, Moschetta JM, Bénard E et al. Noise signature of a MAV rotor in hover. In: *49th 3AF international symposium of applied aerodynamics*, Lille, France, March 2014.
29. Amiet RK. Acoustic radiation from an airfoil in a turbulent stream. J Sound Vib 1975; 41: 407–420.
30. George WK. Lectures in turbulence for the 21st century. Sweden: Chalmers University of Technology, 2013.

31. Fukano T, Kodama Y and Senoo Y. Noise generated by low pressure axial flow fans, I: modeling of the turbulent noise. J Sound Vib 1977; 50: 63–74.
32. Serré R, Gourdain N, Jardin T et al. Aerodynamic and acoustic analysis of an optimized low reynolds number rotor. In: *17th international symposium on transport phenomena and dynamics of rotating machinery*, Maui, Hawaii, December 2017.
33. Lowson MV. The sound field for singularities in motion. Proc R Soc A 1965; 286: 559–572.
34. Mao Y, Xu C and Qi D. Frequency-domain model of tonal blade thickness and loading noise. J Acoust Soc Am 2014; 135: 93–103.
35. Kloet N, Watkins S, Wang X et al. Drone on: a preliminary investigation of the acoustic impact of unmanned aircraft systems (UAS). In: *24th international congress on sound and vibration*, London, United Kingdom, July 2017.
36. Kulfan BR. Universal parametric geometry representation method. J Aircraft 2008; 45: 142–158.
37. Deb PAAS K and Meyarivan T. A fast and elitist mutliobjective genetic algorithm. IEEE Transac Evolut Comput 2002; 6: 182–197.
38. Brandt JB and Selig MS. Propeller performance data at low Reynolds numbers. In: *49th AIAA aerospace sciences meeting*, Orlando, Florida, January 2011. [AIAA-2011-1255].
39. Leishman JG. Principles of helicopter aerodynamics. Cambridge: Cambridge University Press, 2002.
40. George AR and Chou ST. Comparison of broadband noise mechanisms, analyses, and experiments on rotors. J Aircraft 1984; 21: 583–592.
41. Chaitanya P, Joseph P, Narayanan S et al. Performance and mechanism of sinusoidal leading edge serrations for the reduction of turbulence-aerofoil interaction noise. J Fluid Mech 2017; 818: 435–464.
42. Serré R, Gourdain N, Jardin T et al. Analysis of the flow produced by a low-Reynolds rotor optimized for low noise applications. part II: acoustics. In: *43rd European rotorcraft forum*, Milan, Italy, September 2017.
43. Bronz M. *A contribution to the design of long endurance mini unmanned aerial vehicles*. PhD Thesis, Institut Supérieur de l'Aéronautique et de l'Espace-ISAE, France, 2012.